SKB P-25-05

ISSN 1651-4416
ID 2082056
November 2025

POSKBAR - Bentonite Erosion Project. Integration of salinity dependent wall friction and particle aggregate sedimentation in the quantification of bentonite erosion

Arnau Pont, Virginia Cabrera
POSKBAR

Summary

In this report, the general principles and guidelines from the previous phases of the project (Pont et al., 2020, Pont and Idiart, 2022 and Pont, 2023) regarding the numerical modelling of bentonite expansion erosion and sedimentation are further developed. The model developed by Neretnieks et al. (2009), Liu et al. (2009) and Moreno et al. (2010) led to unbounded expansion, which is something that has not been observed in small-scale experiments using narrow artificial fractures. For this reason, an extension to this model accounting for wall friction and sedimentation have been implemented in COMSOL Multiphysics® and extensively tested with relevant experimental data.

The first improvement concerns the thickness of the sol region, which depends on the wall friction term in the smectite transport equation. This thickness must be related to the sodium concentration to accurately describe cases with fracture flow or sloping fractures. To address this, an empirical correlation for general use with the three bentonites considered (MX-80, Nanocor and Bara-Kade) have been derived.

Also, the previous sedimentation model has been improved to properly describe erosion in sloping fractures. The definition of a proper correlation between particle aggregate size and fracture aperture is one of the most relevant aspects to be considered in the prediction of the long-term erosion rate in non-horizontal fractures. In this sense, the reference particle aggregate diameter has been revised, as well as the sedimentation velocity function in narrow fractures (Neretnieks and Moreno, 2018).

Then, the model has been validated with all experiments already considered by Pont (2023) together with a new set of experimental data covering a wide range of relevant scenarios, obtaining a good agreement between experimental and numerical results.

Finally, the complete model has been upscaled to realistic repository conditions, simulating the KBS-3 concept bentonite buffer intersected by a single fracture with two different orientations, either horizontal or vertical. Several sodium concentrations, flow velocities and fracture apertures have been tested to provide a preliminary assessment of the long-term buffer performance. This assessment has focused on deriving correlations between the erosion rate and sodium concentration, fracture aperture and flow velocity when glacial groundwater intrudes the bentonite buffer.

Table of Contents

1 Introdcution

In the previous phase of the POSKBAR Bentonite Erosion project (Pont, 2023), a numerical model accounting for wall friction, flow erosion, and sedimentation due to gravity was developed and partially validated with experimental data corresponding to small-scale tests corresponding to the BENERO project (CIEMAT, 2020) and Schatz et al. (2013). The model was also upscaled to a single buffer 3D geometry intersected by a horizontal fracture. Based on this model, a regression equation for the long-term erosion rate was derived in terms of the fracture aperture and the flow velocity. Unlike the previous results of this kind obtained by Neretnieks et al. (2010, 2017), a quadratic dependence on the fracture aperture was found due to the effect of wall friction, whereas a linear correlation with flow velocity was obtained.

The present report constitutes a further development of the model of bentonite expansion, erosion, and sedimentation in the framework of the POSKBAR project. In this fourth stage, the model has been improved with (i) an empirical correlation between wall friction at the rim and sodium concentration, and (ii) a more robust sedimentation model, which will allow a more realistic assessment of cases with fracture flow and sloping fractures, and a more accurate estimation of the long-term erosion rate in large-scale buffer models. Regarding the first numerical implementation, all small-scale tests that were modeled in the previous phase of the project (Pont, 2023) have been simulated again (Section 2) for validation, and five more cases from CIEMAT and Schatz and Akhanoba (2017) have been included as well for analyzing the sensitivity in terms of initial bentonite dry density and fracture slope, respectively.

Regarding the refinement of the sedimentation model, the reference particle aggregate diameter has been revised and a differentiated law for the sedimentation velocity in narrow fractures has been implemented (Neretnieks and Moreno, 2018). These features have been applied to all cases with sloping fractures considered in the previous phase of the project (Pont, 2023) and to a new set of 5 cases with 0.1 mm vertical fractures from Hedström et al. (2023) and the DilBi I series described in Pont and Idiart (2022). This special focus on narrow sloping fractures aims at understanding the physical mechanisms that lead to very limited erosion. Altogether, 24 cases (Table 2-1) have been considered for the validation of the presented model updates (Section 3) and the corresponding results are presented in Section 5.

In Section 6 the model is applied to the Performance Assessment of the bentonite buffer in the KBS-3 repository under the effect of a single intersecting fracture with flowing glacial meltwater. The final goal consists in providing a best estimate of the buffer degradation process in critical scenarios involving water salinity below CCC and low calcium sorption. As observed in small-scale tests, these chemical conditions can lead to significant clay mass losses, but the upscaling to repository dimensions assuming normalized erosion rates per unit surface of buffer-fracture interface is not straightforward, as it leads to very conservative results due to large differences in terms of evolving buffer density and composition, among others . Chemical erosion of the buffer is, together with unbounded expansion, one of the major concerns in the long-term safety assessment of a KBS-3 repository. It refers to the decomposition of smectite into colloids due to the presence of groundwater with ionic strength below CCC, and the subsequent material loss because of flow drag or gravity. In this sense, SKB (2004) proposed a mass balance approach for estimating the buffer erosion rate assuming an equivalent flow rate (Q_{eq}) and the dilution of calcite, leading to values ranging from 0.0032 to 0.4 kg·yr^{-1} (3000 to 375,000 years up to loss of integrity damage) depending on the initial calcite concentration. On the other hand, Liu and Neretnieks (2006) revised the previous model assuming real flow rates and replacing calcite by gypsum (0.7 wt. %), which is considered the real driver of calcium concentration in the buffer. In this case, buffer performance was expected to deteriorate beyond 11,000 years according to Arthur (2011), who carried out a review of chemical erosion conceptual models. However, the SR-Can Safety Assessment (SKB, 2006) considered only pure-Na montmorillonite, which is also the focus of the present work. Three different hydrogeological models were considered – continuous porous medium (CPM), fully correlated discrete fracture network (DFN) and semi-correlated DFN, being the latter the worst case with 35 % of the deposition holes affected by erosion after 25,000 years (Arthur, 2011).

Nowadays, these results are considered rather conservative. In recent years, significant efforts have been devoted to the development of small-scale laboratory tests. A significant resistance to bentonite expansion and erosion was observed in these tests when reproducing the conditions that can lead to an unstable gel. The presence of wall friction and fracture partial clogging due to the formation of secondary gel from flocs formed by the reassembly of detached colloids (Neretnieks et al., 2018) requires an extension of the best-estimate numerical models. At the same time, the erosion rate predicted by the coupled model in Neretnieks et al. (2009) was exceeded in one or two orders of magnitude by the upscaling to repository conditions performed with laboratory tests by Smith et al. (2017), who estimated that erosion rates of 1 $kg \cdot yr^{-1}$ may be reached in 4 % of the supercontainer sections in the KBS-3H repository concept in Olkiluoto after 1000 years of glacial conditions, although several uncertainties still needed to be addressed.

In Pont (2023) an unclear correlation between erosion rate and sodium concentration in water was obtained in the buffer-scale model with a single intersecting horizontal fracture. The main reason behind this outcome was that the rheological model applied to the calculation of shear resistance at the rim did not take the salinity of water into account (Pujala, 2014 and Neretnieks et al., 2018). This prevented the diffusion of a higher quantity of dilute sol through the rim when the sodium concentration decreased as empirically observed. In this sense, the present work aims at extending the parametric simulation carried out by Pont (2023) for the quantification of the long-term erosion rate in a realistic buffer geometry crossed by a single horizontal fracture. Apart from analysing the correlation with fracture aperture and flow velocity, the sensitivity respect to sodium concentration in water will also be quantified (Section 6). Furthermore, the model will also be applied to single vertical fractures with a fixed flow velocity. Finally, in Section 7 the main conclusions are listed together with the limitations of the model and the next steps to be taken for an accurate estimation of the long-term erosion rate in both horizontal and sloping fractures.

2 Methodology

The bentonite expansion, erosion and sedimentation model consists of a coupled multiphysics system, characterized by three governing equations: sodium cation transport, smectite expansion, and flow dynamics. All of them are solved in the computational platform COMSOL Multiphysics version 6.1 (COMSOL, 2023) based on the finite element method and a staggered coupling scheme, which solves the three equations sequentially up to convergence in the above-mentioned order.

The validation process consisted in the simulation of 24 small-scale tests. These experimental tests come from different laboratories reported by Schatz et al. (2013), Schatz and Akhanoba (2017), Pont and Idiart (2022), Hedström et al. (2023) and several experimental tests from CIEMAT (2022). The list accounts for three types of experimental tests: extrusion, erosion, and sedimentation. Their main characteristics are outlined in Table 2-1. The extrusion tests were carried out at two different dry densities for each montmorillonite (1700 and 1400 kg/m3 for Nanocor® and 1591 and 1400 kg/m3 for MX-80), and also, for different fracture apertures. The main variable in the erosion tests is the flow rate. Its effect on bentonite expansion and mass loss is studied at three different fracture apertures for a low flow rate in the case of Nanocor®, and at two different flow rates for the MX-80. Sedimentation tests are performed assuming a non-horizontal slope for different fracture apertures in the case of the Nanocor®. In turn, sedimental test for MX-80 study the effect of the fracture slope as well as the combined effect of water flow through the fracture. Finally, the erosion and sedimentation patterns of MX-80 and Bara-Kade in narrow vertical fractures are studied for a better understanding of the low erosion rates observed in these experiments. Note that the cations of the saline infiltration water [Na^+] are of the same type as the cations compensating the structural charge of the sodium-montmorillonite. Hence, no ion exchange is occurring in these systems.

In Section 6, the methodology for the quantification of the long-term erosion rate in a KBS-3 buffer intersected by a single horizontal fracture in terms of flow velocity, fracture aperture and sodium concentration in water (Section 5) has consisted in the simulation of all possible parametrizations in a large scale geometry given three relevant values for each variable (27 cases):

Fracture aperture: $\delta_1 = 0.2$ mm, $\delta_2 = 0.6$ mm, $\delta_3 = 1$ mm

Flow velocity: $v_1 = 10^{-7}\ m \cdot s^{-1}$, $v_2 = 5 \cdot 10^{-7}\ m \cdot s^{-1}$, $v_3 = 10^{-6}\ m \cdot s^{-1}$

Sodium concentration: $c_1 = 1$ mM, $c_2 = 4$ mM, $c_3 = 8$ mM

A fixed value for the initial bentonite dry density of 1600 $kg \cdot m^{-3}$ has been assumed in all cases, as well as homogeneous isotropic smectite diffusion in the buffer. A similar approach has been taken for the application to a single vertical fracture. In this case, a fixed inlet flow velocity value of $10^{-7}\ m \cdot s^{-1}$ has been considered in order to have a clear insight on the mass losses due to sedimentation:

Fracture aperture: $\delta_1 = 0.1$ mm, $\delta_2 = 0.2$ mm, $\delta_3 = 0.4$ mm

Sodium concentration: $c_1 = 1$ mM, $c_2 = 4$ mM, $c_3 = 8$ mM

Table 2-1. List of simulated tests for model validation with its main characteristics.

Bentonite type	**Exp. test**	**Case**	**Dry density [kg/m^3]**	**Initial radius [cm]**	**$[Na^+]$ [mM]**	**Water inlet velocity [m/s]**	**Fracture aperture [mm]**	**Fracture slope (º)**	**Duration [d]**	**Ref.**
Nanocor®	*Extrusion*	Case 1	1700	0.95	1	0	0.1	0	30	[a] # 22
		Case 2	1700	0.95	1	0	0.45	0	30	[a] # 23
		Case 3	1700	0.95	1	0	0.36	0	30	[a] # 24
		Case 4	1400	0.95	1	0	0.1	0	30	[a] # 22B
		Case 5	1400	0.95	1	0	0.45	0	30	[a] # 23B
		Case 6	1400	0.95	1	0	0.36	0	30	[a] # 24B
	Erosion	Case 7	1400	0.95	1	1.50×10^{-6}	0.1	0	60	[a] # 27
		Case 8	1400	0.95	1	5.41×10^{-7}	0.45	0	60	[a] # 28A
		Case 9	1400	0.95	1	4.08×10^{-7}	0.36	0	60	[a] # 28B
	Sedimentation	Case 10	1400	0.95	1	0	0.1	90	30	[a] # 14
		Case 11	1400	0.95	1	0	0.45	90	30	[a] # 15
		Case 12	1400	0.95	1	0	0.36	90	30	[a] # 16
NaMt (MX-80)	*Extrusion*	Case 13	1591	1	DI	0	1	0	30	[b] # 11
	Erosion	Case 14	1591	1	DI	2.00×10^{-4}	1	0	19	[b] # 3
		Case 15	1591	1	DI	2.60×10^{-5}	1	0	28	[b] # 5
		Case 16	1400	1	DI	6.00×10^{-6}	0.1	0	30	[c] # 2a
	Sedimentation	Case 17	1400	1	DI	6.00×10^{-6}	0.1	45	30	[c] # 2b
		Case 18	1400	1	DI	6.00×10^{-6}	0.1	90	30	[c] # 2c
		Case 19	1420	1.75	1	3.06×10^{-5}	0.1	90	63	[d] # 1
		Case 20	1420	1	1	3.06×10^{-5}	0.1	90	63	[d] # 2
		Case 21	1100	1	1	3.96×10^{-5}	0.1	90	63	[d] # 5
Bara Kade	*Sedimentation*	Case 22	1420	1.75	1	0	0.1	90	210	[e] # 1
		Case 23	1420	1.75	20→1	6.80×10^{-6}	0.1	90	210	[e] # 4
		Case 24	1420	1.75	1	4.77×10^{-5}	0.1	90	77	[e] # 8

DI = deionized water
[a] CIEMAT (2022)
[b] Schatz et al. (2013)
[c] Schatz and Akhanoba (2017)
[d] Pont and Idiart (2022)
[e] Hedström et al. (2023)

3 Conceptual model and governing equations

The model presented by Pont (2023) is being extended with two main features: (i) a correlation between wall friction and sodium concentration at the bentonite-water interface, and (ii) a more refined sedimentation model for sloping fractures. These two developments are intended to provide a more realistic estimate of bentonite extrusion, erosion and sedimentation. Due to the lack of experimental data, both models have been parametrized and adjusted empirically for a wide range of conditions in Section 3.1.

3.1 Correlation between shear resistance due to non-expansive gel and sodium concentration at the rim

The shear resistance velocity $\vec{w}$ has been restricted to the rim concentration φ_{rim}, which has been set to 0.01 assuming that no yield stress is observed below 3 % wt. (Neretnieks and Moreno, 2018). In other words, it is the lowest smectite volume fracture to yield shear resistance against extrusion, and the one which will provide more viscous friction according to the definition of $\vec{w}$ (equation 1). In fact, it is a virtual velocity that quantifies the resistance to extrusion. For consistency with viscous friction, $\vec{w}$ is defined as the average velocity of a viscous laminar flow between two parallel plates, as if wall friction, τ_{fric}(Pa), was the driving traction

$$\vec{w} = \frac{\tau_{\mathrm{fric}}\delta}{4\eta_{\mathrm{eff}}} \tag{1}$$

where δ (m) is the fracture aperture. τ_{fric} represents the shear resistance exerted by the segregated gel at the expanding bentonite-water interface due to the confinement in the fracture. Although the swelling pressure of the expanding paste will always overcome the yield stress of this dilute gel τ_0 (Pa), the surface integral of the shear stress after mobilization, from now on τ_1 (Pa), will increase with the extrusion radius as the gel accumulates. Eventually, it may lead to a limitation of extrusion as observed in several small-scale tests below CCC. On the other hand, the strain rate at this region is expected to be several orders of magnitude lower than the typical values of $\dot{\gamma}_0$, which depends on the clay type and its aging, and will be calibrated in Section 4.3. This should not be confused with the behaviour of the swelling paste, which expands due repulsion forces while water is suctioned in the opposite direction (Neretnieks et al, 2009). Although initially the motion of the segregated gel at the rim might be driven by swelling pressure overcoming $\dot{\gamma}_0$, the deformation rate will soon slow down until an equilibrium is reached. For this reason, a quasistatic approximation is assumed for both τ_1 and η_{eff}, so that wall friction velocity can be written as

$$|\vec{w}| = \frac{\tau_1\,\delta}{4\eta_{\mathrm{eff}}}\xi(r,r_{rim})\varsigma(r_{rim})\zeta(\delta) = \frac{k_{HB}|\dot{\gamma}_0|^n\,\delta}{4(\tau_0|\dot{\gamma}_0|^{-1}+k_{HB}|\dot{\gamma}_0|^{n-1})}\left(\frac{r-r_0}{r_{rim}-r_0}\right)^{\beta}\left(\frac{r_0}{r_{rim}}\right)\left(\frac{\delta_0}{\delta}\right)^{-1+n^{-1}} \tag{2}$$

where δ(m) is the fracture aperture, r(m) is the expansion radius, η_{eff}(Pa·s) is the effective viscosity of the smectite at the rim, $\dot{\gamma}_0$(s^{-1}) is the yield strain rate and k_{HB} and n are parameters of the Herschel-Bulkley rheological model (Pujala, 2014). As conceived by Pont and Idiart (2022), $\vec{w}$ is the virtual average laminar flow velocity between two plates caused by the action of shear stress at the rim. The resulting field is convoluted by three functions: on one hand ξ restricts $\vec{w}$ near the rim in a sufficiently regular way so it does not compromise continuity in the finite element space. In this sense, β determines the thickness of the shear bearing region, which is expected to increase with lower sodium concentration, together with the amount of dilute sol that will diffuse through the rim (chemical erosion). For this reason, β and $\dot{\gamma}_0$ have been expressed in terms of sodium concentration at the rim

$$\beta = Ac_{\mathrm{rim}}{}^{\mathrm{a}}, \tag{3a}$$

$$\dot{\gamma}_0 = B\left(\frac{c_{\mathrm{rim}}}{CCC}\right)^{b}, \tag{3b}$$

where c_{rim} (mol·m^{-3}) is the sodium concentration at the bentonite-water interface, CCC (mol·m^{-3}) is the Critical Coagulation Concentration (~ 4 mM for sodium bentonites), and a, A, b and B are parameters to be calibrated for each bentonite type. On the other, ς reduces $|\vec{w}|$ proportionally with the extrusion distance, since the detached material must fill a longer perimeter, and finally ζ establishes a correlation with the fracture aperture accordingly with the index *n* of the Herschel-Bulkley rheological model. Taking the widest fracture considered in the calibration ($\delta_0 = 1$ mm) as reference, the relevance of $\vec{w}$ becomes stronger as δ gets smaller. In a linear flow, the strain rate at the centre of the fracture would depend linearly on δ (parabolic velocity profile), but equation 4 shows that in a Herschel-Bulkley flow the velocity profile v_{HB} follows a slightly different dependence (Neretnieks and Moreno, 2018)

$$v_{HB} = \frac{2\delta}{\frac{1}{n}+2}\left(\tau_1 \frac{\delta}{k_{HB}}\right)^{\frac{1}{n}} = \frac{2\delta}{\frac{1}{n}+2}\left(|\dot{\gamma}|^n \delta\right)^{\frac{1}{n}} \sim \delta\left(\delta^{-n}\delta\right)^{\frac{1}{n}} = f\left(\delta^{\frac{1}{n}}\right) \tag{4}$$

Equation 4 assumes therefore that the strain rate is proportional to $\delta^{-1+n^{-1}}$, for which ζ will be proportional to $\delta^{1-n^{-1}}$. It is noted that the current formulation does not yield a linear relation between extrusion and fracture aperture, as in the method proposed by Börgesson et al. (2018).

Regarding boundary conditions, closed walls (i.e., zero concentration gradient in the normal direction) are prescribed on all model contours except the fracture inlet and outlet, where an infinitesimal smectite volume fraction (non-zero value) and an open boundary condition are imposed, respectively. Initially, the fracture domain is assigned the same infinitesimal smectite concentration (clean water), whereas the initial bentonite pellet domain is given the volume fraction corresponding to its dry density.

The model (equation 2) is completed with a proper parametrization for each kind of bentonite (equation 3). This includes the calibration of six parameters corresponding to the yield strain rate *B* (s^{-1}) in equation 3b, the exponent of the Herschel-Bulkley rheological model *n* and the correlation between wall friction and sodium concentration at the rim (*a*, *A*, *b*) in equations 3a and 3b. As shown in Table 3-1, the parametrizations for the three considered bentonites in the validation process (MX-80, Nanocor and Bara-Kade) do not show significant differences:

Table 3-1. Parametrization of the three different considered bentonite types for the validation of the model.

Bentonite type	**n**	**a**	**A**	**b**	**B [s^{-1}]**
MX-80	0.45*	0.5	4	0.1	0.055
Nanocor	0.48	0.5	2.5	0.1	0.051
Bara Kade	0.48	0.5	2	0.1	0.040

*Neretnieks and Moreno (2018)

All parametrizations have been calibrated based on their effect on expansion, erosion and sedimentation, for which they are conceived for general use. Only parameters *a* and *b* should be further calibrated with a wider range of sodium concentrations for the Nanocor and Bara-Kade bentonites, since nearly all of the experiments have been performed with a single 1 mM concentration.

3.2 Fluid mechanics: fracture flow

Flows where advective inertial forces are negligible in front of the viscous ones (*Re*<<1, with *Re* being the Reynolds number), are usually represented by the Stokes equations. Given the clear segregation between gel and sol in terms of rheological behaviour, this approach would perfectly allow the description of water and sol motion in a clean fracture. However, this approach would not apply to sloping fractures, where the gravity force is expected to detach flocs form the expanded disc. In this case, drag forces become relevant, but they are not accounted for in the Stokes equations. For this reason, Darcy's law has been used in all cases.

3.2.1 Darcy's law

Darcy's law for a weakly compressible flow is shown in equations 5a-b, where $\rho = \varphi\rho_s + (1-\varphi)\rho_w$ is the water-bentonite mixture density (kg·m^{-3}), ρ_s and ρ_w are the solid (or grain) and water densities (kg·m^{-3}), respectively, $\vec{u}$ is the velocity (m·s^{-1}), p is the pressure (Pa), $\vec{g}$ is the gravity acceleration vector (m·s^{-2}), η_w (Pa·s) and η_{rel} (-) are the water and the relative viscosity, respectively, and $\nabla^S\vec{u}$ (s^{-1}) is the strain rate (∇^S being the symmetric gradient), also referred to as $\dot{\gamma}$ (s^{-1}).

$$\vec{u} = -\kappa(\eta_w\eta_{\text{rel}})^{-1}(\nabla p - \vec{g}(\rho - \rho_w)) \tag{5a}$$

$$\partial_t\rho + \nabla\cdot(\rho\vec{u}) = 0 \tag{5b}$$

$$\eta_{\text{rel}} = 1 + 1.022\varphi_{\text{cov}} + 1.358{\varphi_{\text{cov}}}^3 \tag{5c}$$

$$\kappa = \frac{\delta^2}{12} \tag{5d}$$

The proposed model is only solved in the outer domain (beyond the rim) of the decomposition presented by Pont (2023), since flow erosion is only expected to affect the outermost dilute phase (sol), which may interact with seeping water and move accordingly as shear driven slurry. Due to the sharp viscosity increase with smectite volume fraction, denser expanding paste in the bentonite disc will not be altered by the shear force of seeping water flow. Smectite sol below 3 % wt., unlike flocs or gel, is a Newtonian fluid with a well-known viscosity correlation (equation 5c) in terms of the smectite co-volume φ_{cov}(-) (Appendix A) and sodium concentration (Adachi et al., 1998). According to Moreno et al. (2010), φ_{cov} should be limited to 130 % of the coin volume based on the available experimental data. Also, a cubic law for the permeability has been assumed for horizontal fractures (equation 5d).

As boundary conditions, a no-slip condition (i.e., zero velocity) is prescribed on all model contours except the symmetry planes, where a zero-flux boundary condition applies, and the fracture inlet and outlet, where a flow velocity (Table 2-1) and zero pressure are imposed, respectively (Figure 4-1). The flow initial conditions were derived with a stationary solution of the Darcy equations accounting for the described boundary conditions.

3.2.2 Sedimentation model in sloping fractures

Equation 6a shows de settling velocity of thin smectite sheets (Neretnieks et al., 2017), derived from the equilibrium between gravity, drag and buoyancy. This terminal motion can be translated into equation 5a by considering a virtual permeability κ (equation 6b) with the average particle aggregate diameter modelled in equation 6c.

$$u_p = \frac{g(\rho-\rho_w){d_p}^2}{18\eta_w} \tag{6a}$$

$$\kappa = \frac{\eta_{\text{rel}}{d_p}^2}{18} \tag{6b}$$

$$d_p = d_{p0}\left(\frac{\delta}{\delta_0}\right)^{\alpha} \tag{6c}$$

The average particle aggregate diameter for apertures with $\delta \geq \delta_0$ (free sedimentation) is taken as 35 μm. Neretnieks and Moreno (2018) observed deviations from the expected cubic law between mass loss rate and aperture in vertical fractures ranging from 0.1 mm to 1 mm, whereas Neretnieks et al. (2017) found a quadratic dependence of the settling velocity of large coin-like agglomerates with 1 % by volume smectite in a vertical slit respect to the aperture. In the present case, a cubic law has been used for $\delta > 0.1$ mm and a quadratic one for the rest. Since velocity depends on ${d_p}^2$, the parameter α in equation 6c would be 3/2 in the first case, and 1 in the latter. The correlation between particle diameter and fracture aperture is of crucial importance for describing the low erosion rates observed in 0.1 mm fractures, where the motion and the size of smectite flocs is strongly constrained by the walls. This can lead to the formation of a secondary gel which might even clog the fracture (Neretnieks and Moreno, 2018).

Another important issue has been the interaction between flow erosion and sedimentation. Experimental tests carried out by Leal Olloqui et al. (2024) and Hedström et al. (2023) showed that sedimentation is a transient phenomenon that stops after few days. Moreover, experiments performed by CIEMAT in the framework of the Benero project considering different flow directions within the fracture have shown that the erosion rate reaches a minimum when water flows in the direction of gravity (no additive effect). For this reason, the present work limits the inlet flow velocity to the particle sedimentation velocity in equation 6a.

4 Numerical model

4.1 Model geometry

4.1.1 Small scale tests

The extrusion, erosion and sedimentation in sodium montmorillonite were studied using the experimental setup illustrated in Figure 4-1. The setup consisted of small-scale, flow-through artificial fracture cells. The fracture was filled with low salinity water between two plates that holds a hole for a pellet of compacted bentonite. The set up can be positioned at different angles, to carry out experiments with different fracture slope. The dimensions of the different components used in the experimental setups in Schatz et al. (2013), Schatz and Akhanoba (2017), Schatz (2020), Pont and Idiart (2022) and CIEMAT (2022) are summarized in Table 4-1.

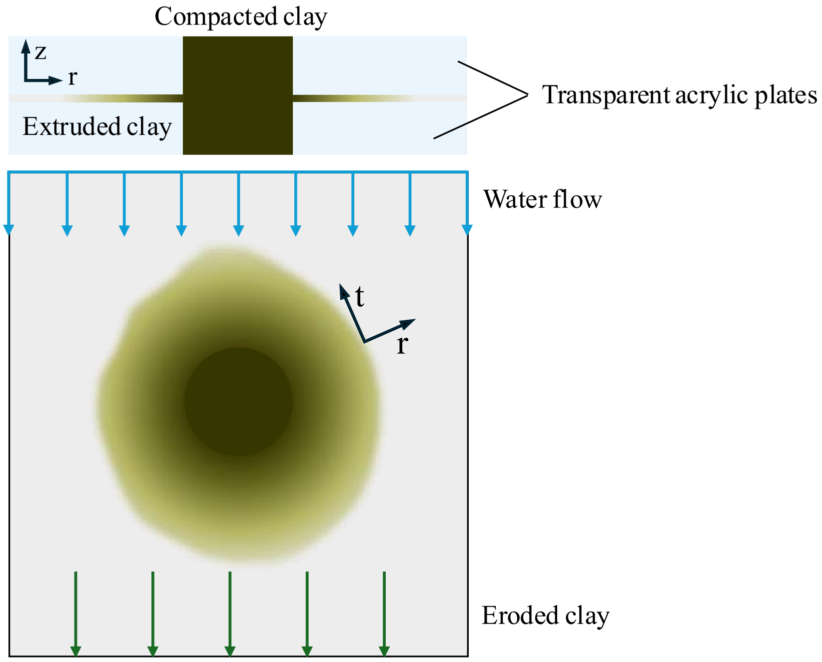

Figure 4-1. *Schematic conceptual model with a planar fracture cutting through a cylindrical bentonite pellet (Neretnieks et al., 2017) showing the radial (r), tangential (t) and vertical (z) directions of the 3D domain.*

Table 4-1. Main features of the different setups corresponding to the small-scale bentonite erosion simulation cases in Section 4.

Tests (reference)	Fracture size [cm]	Pellet shape	Pellet height [cm]	Pellet outer diameter [cm]	Pellet inner diameter [cm]
CIEMAT (2022)	17 x 17	cylinder	1	1.9	-
Schatz et al. (2013) Schatz and Akhanoba (2017)	24 x 24	cylinder	2	2	-
Pont and Idiart (2022) Hedström et al. (2023)	17 x 17	hollow cylinder	1	3.5	1.5

4.1.2 Repository conditions

For the long-term buffer integrity evaluation analysed in Section 5, a geometrical setup composed by the reference 3D geometry of the installed KBS-3 buffer (SKB, 2011) together with a single horizontal or vertical fracture 5.5 m x 8 m (Sena et al., 2010) with different fracture apertures has been implemented (Figure 4-2).

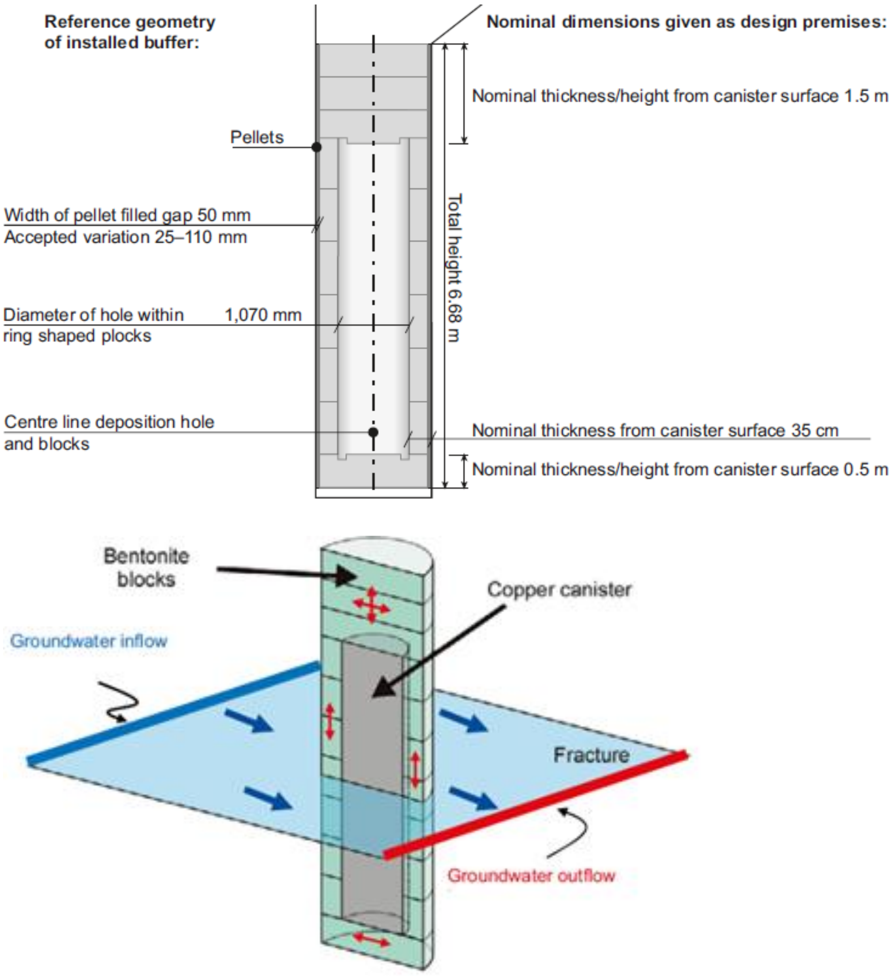

Figure 4-2. Dimensions of the buffer in the KBS-3 repository (SKB, 2011) and schematic representation of a horizontal fracture crossing the bentonite buffer (Sena et al, 2010).

4.2 Computational model

A three-dimensional representation of the experimental setup shown in Figure 4-1 has been implemented in the COMSOL Multiphysics (COMSOL, 2023) in a 3D geometry. Only a quarter of the original domain has been considered, taking profit from the planar and vertical symmetries. This means considering only half of the fracture thickness and reducing the buffer to a semicylinder, as shown in Figure 4-4. With that, a more refined radial mesh of 50,000-112,000 linear elements has been generated, depending on the fracture aperture (Figure 4-3). Solving the equations in the initial bentonite domain allows a precise calculation of the swelling pressure in the fracture, which might decrease in small-scale tests due to the small size of the sample.

As previously stated, a moving mesh algorithm has been solved for minimizing element distortion caused by the motion of the rim (Γ). Foreseeing the expansion beyond the initial position of the rim (1 cm from the pellet), the interior domain has been carefully refined in order to prevent resolution losses due to the expected element size growth. Despite this extra computational cost, the final version of the model drastically outperformed the previous ones. Except the sedimentation cases, which still need to be refined, the simulation of all other tests has taken less than 1 hour.

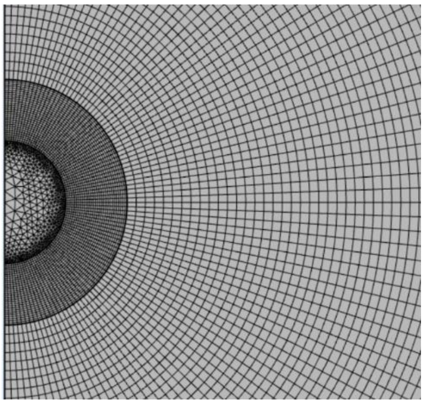

Figure 4-3. *Finite Element mesh in COMSOL. The areas subject to more deformation have been specifically refined.*

Regarding the upscaled model to repository dimensions (Fig. 4-4), the increase in computational cost with respect to the short small-scale tests have limited both mesh refinement and the total simulation time that can be considered. A single simulation up to 100,000 years could be affordable with the last version of the model, but a parametric sweep of 36 cases (Section 6) would be excessively time consuming. From this reason, only 10 years from the onset of glacial meltwater arrival have been considered, up to the time needed for expansion and erosion to reach pseudo-steady state conditions.

Like in the models developed for the small-scale tests, only a quarter of the geometry has been considered due to symmetry, and a radial mesh of linear elements with specific refinement of the expanding region and the initial bentonite-water interface has been generated (Figure 4-4). This has led to a model size ranging from 146,000 to 220,000 elements depending on the fracture aperture.

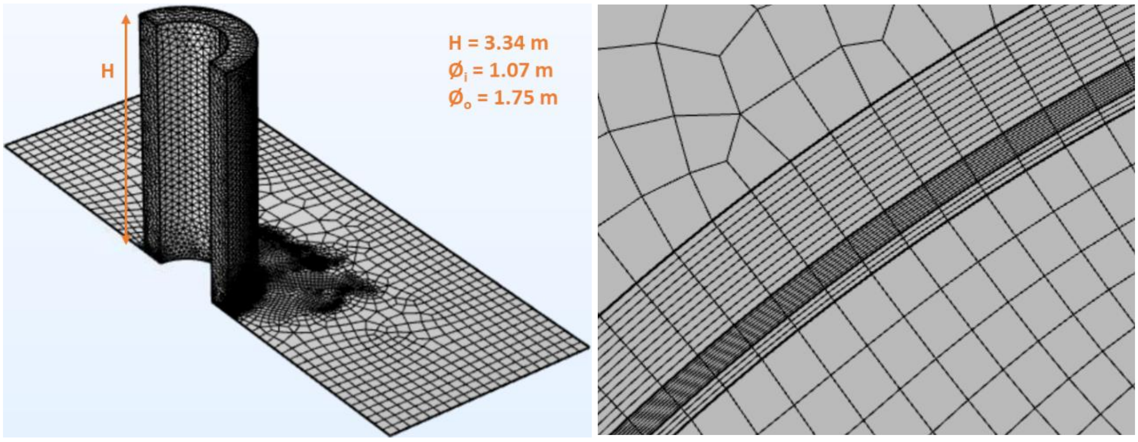

Figure 4-4. *Computation model after considering vertical and fracture midplane symmetries (left). Mesh refinement at the buffer-fracture interface with special focus on the expanding region (right).*

5 Results - Validation of the model

In this section, the main results of the tests described in Table 2-1 in terms of expansion and mass distribution in the pellet and the fracture, including eroded mass, are presented and compared to experimental measurements. A summary is shown in Table 5-1.

Overall, the quantification of the final extrusion is properly predicted by the model in all extrusion, erosion and sedimentation experiments except for Case 14, which was carried out with the highest flow rate, and Case 23, which accounts for an evolving sodium concentration from 20 to 1 mM. Also, the final mass distribution has also been properly approximated for most of the considered scenarios in Table 2-1, except for Case 1, which is being reviewed by CIEMAT, and the sedimentation cases with Nanocor and Bara-Kade bentonite, which underestimate the amount of eroded mass (Figures 5-1, 5-2 and 5-3)

Cases 4, 5 and 6 have no experimental counterpart yet, as they are currently being conducted by CIEMAT with a lower dry density (1400 kg/m^3). However, the model outcomes show a small variation from the results obtained with a dry density of 1700 kg/m^3. Case 10 is also a variation of Cases 11 and 12 with a narrower fracture aperture (0.1 mm) that has not been carried out experimentally.

Finally, a special focus was put on cases with vertical narrow fractures (0.1 mm), in order to study the mechanisms behind the low erosion rates observed experimentally by CIEMAT, Leal Olloqui et al. (2024) and Hedström et al. (2023). In this sense, the model has been able to quantify the total eroded mass in all cases conducted with MX-80 bentonite but has underestimated those with Bara-Kade. However, Fig 5-4 shows how the model has been able to reproduce the transient character of sedimentation, as the red erosion rate curve, which belongs to the only case without flow, decreases monotonically after 50 days. This has also been observed for cases with flow, but the model has not yet managed to describe the phenomenology behind this fact. The interaction between flow erosion and sedimentation is further discussed in Section 7.

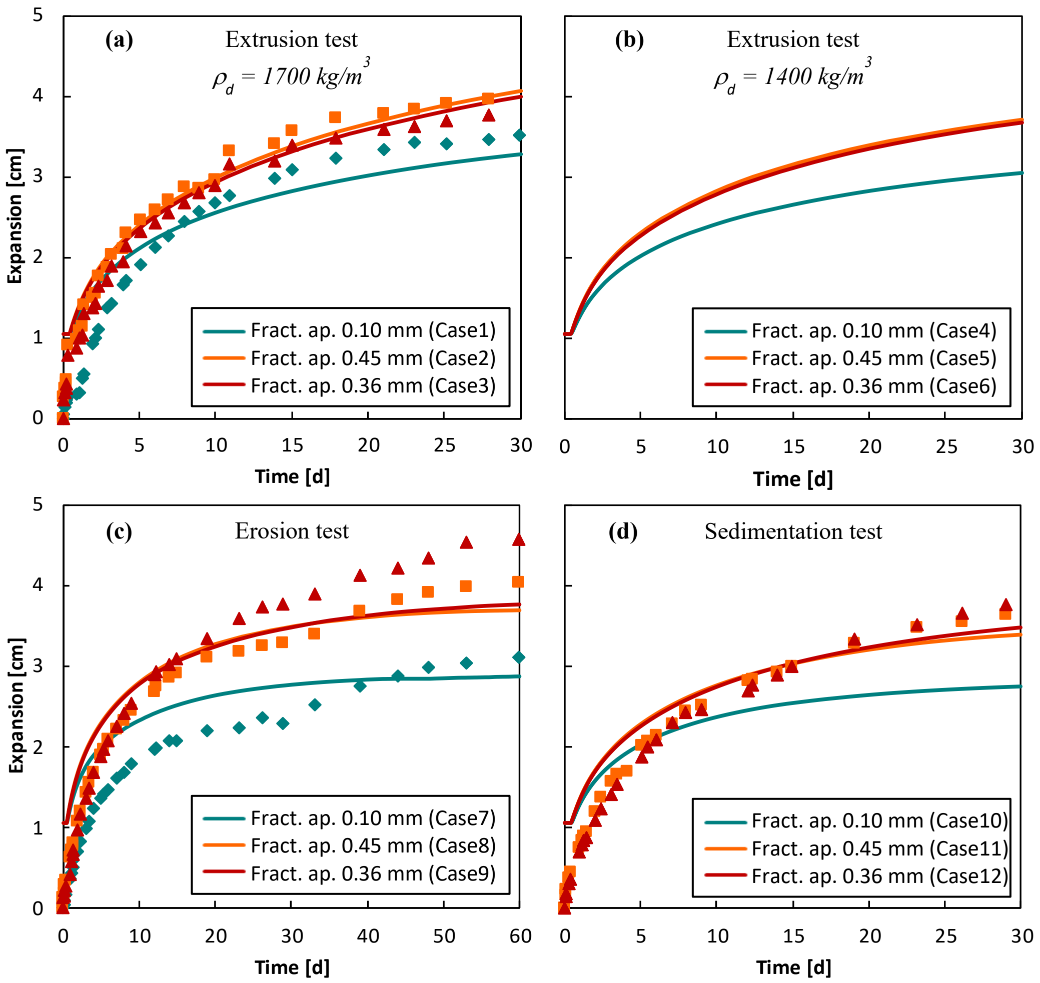

Figure 5-1. *Evolution of expansion radius in Nanocor bentonite for extrusion tests with: (a) ρ_d = 1700 kg/m^3 (Cases 1, 2 and 3) and (b) ρ_d = 1400 kg/m^3 (Cases 4, 5 and 6), (c) erosion tests (Cases 7, 8 and 9) and (d) sedimentation tests (Case 10, 11 and 12). Solid line: model results and markers: experimental data.*

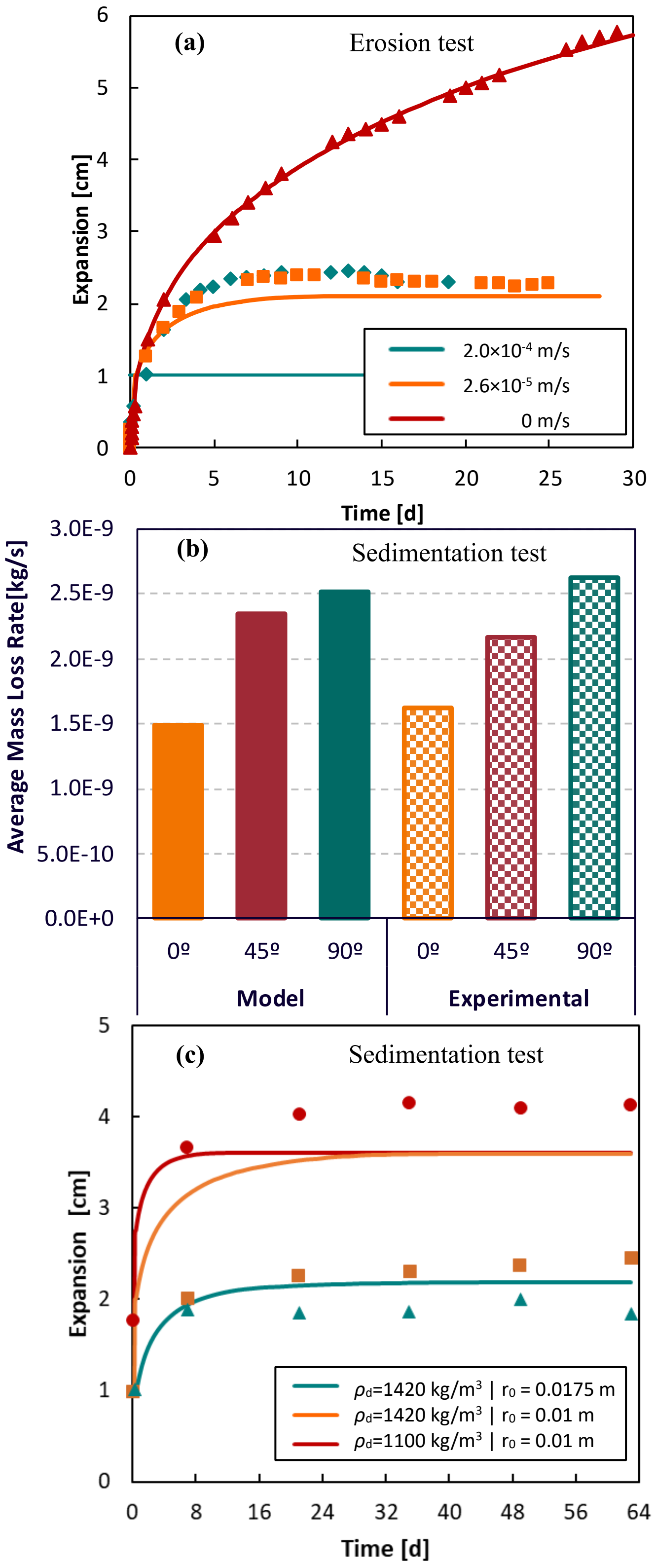

Figure 5-2. *Results of Na-montmorillonite (from Wyoming MX-80 bentonite) samples: (a) Comparison of the temporal evolution of the expansion radius between extrusion (Case 13) and erosion tests (Cases 14 and 15); solid line: numerical results and markers: experimental data. (b) Comparison of the average mass loss rate between erosion (Case 16) and sedimentation tests (Cases 17 and 18). (c) Temporal evolution of the extrusion radius in sedimentation test with flow (Cases 19, 20 and 21); solid line: numerical results and markers: experimental data.*

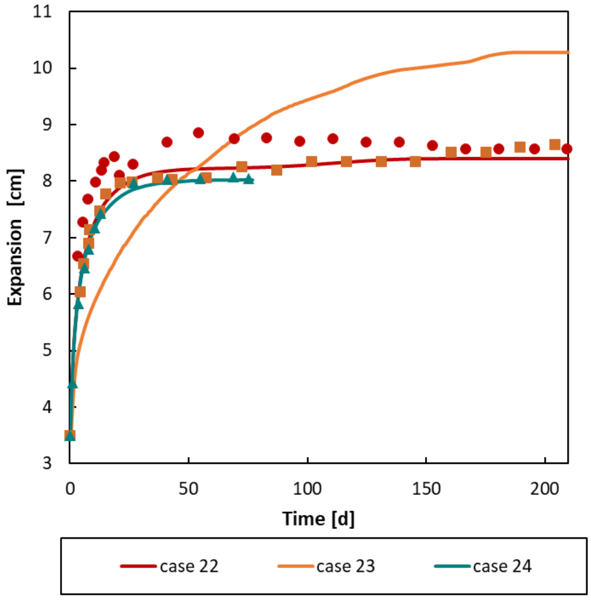

Figure 5-3. *Evolution of expansion diameter in Bara-Kade bentonite for sedimentation test (cases 22, 23, and 24). Solid line: model results and markers: experimental data.*

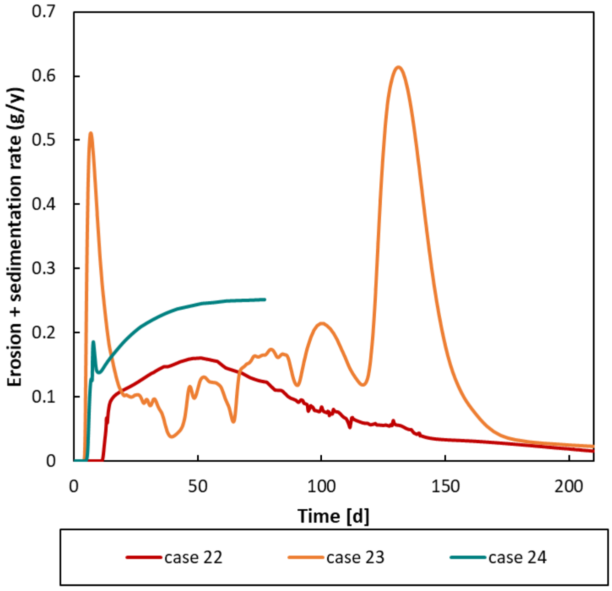

Figure 5-4. *Evolution of the total mass loss rate in Bara-Kade bentonite for sedimentation test (cases 22, 23, and 24) calculated with the model*

.

Table 5-1. Main results in terms of bentonite expansion and final mass balance for the validation cases.

Bentonite type	Exp. test	#case	Expansion radius [cm]		Extruded mass [g]		Eroded mass [g]		% Eroded mass		Ref
			Experimental	Numerical	Experimental	Numerical	Experimental	Numerical	Experimental	Numerical	
Nanocor	Expansion	Case 1	3.506	3.271	1.296	0.325	0.0	0.0	-	-	[a] # 22
		Case 2	3.951	4.062	1.820	1.600	0.0	0.0	-	-	[a] # 23
		Case 3	3.768	3.994	1.488	1.312	0.0	0.0	-	-	[a] # 24
		Case 4	-	3.058	-	0.270	0.0	0.0	-	-	[a] # 22B
		Case 5	-	3.709	-	1.271	0.0	0.0	-	-	[a] # 23B
		Case 6	-	3.680	-	1.058	0.0	0.0	-	-	[a] # 24B
	Erosion	Case 7	3.093	2.864	0.543	0.250	0.165	0.10	4.0	2.5	[a] # 27
		Case 8	4.023	3.682	0.708	1.240	0.404	0.28	10.2	7.1	[a] # 28A
		Case 9	4.565	3.753	0.863	1.090	0.284	0.20	7.2	4.9	[a] # 28B
	Sedimentation	Case 10	-	2.751	-	0.240	-	0.03	-	0.7	[a] # 14
		Case 11	3.656	3.404	0.886	1.151	0.538	0.12	13.6	3.0	[a] # 15
		Case 12	3.773	3.496	0.869	1.009	0.285	0.043	7.2	1.1	[a] # 16
MX-80	Expansion	Case 13	5.842	5.736	4.492	4.872	-	-	-	-	[b] # 11
	Erosion	Case 14	2.295	-	0.684	0.289	4.730	5.3	47.2	53.0	[b] # 3
		Case 15	2.274	2.094	1.663	0.960	3.437	3.9	34.4	38.8	[b] # 5
		Case 16	-	3.268	-	2.068	-	2.5	41.5	25.5	[c] # 2a
	Sedimentation	Case 17	-	1.389	-	0.397	-	6.2	68.7	62.2	[c] # 2b
		Case 18	-	1.420	-	0.411	-	6.1	59.6	61.5	[c] # 2c
		Case 19	4.135	1.854	0.279	0.260	-	0.18	2.5	1.6	[d] # 1
		Case 20	2.447	2.590	-	0.268	-	0.17	2.0	3.2	[d] # 2
		Case 21	1.843	2.184	-	0.174	-	0.17	1.3	4.1	[d] # 5

Bentonite type	Exp. test	#case	Expansion radius [cm]		Extruded mass [g]		Eroded mass [g]		% Eroded mass		Ref
			Experimental	Numerical	Experimental	Numerical	Experimental	Numerical	Experimental	Numerical	
Bara-Kade	Sedimentation	Case 22	4.300	4.200	0.350	0.445	0.670	0.194	6.000	1.74	[e] # 1
		Case 23	4.350	5.150	0.360	0.694	0.710	0.186	6.364	1.67	[e] # 4
		Case 24	4.000	4.000	0.300	0.406	0.260	0.156	2.330	1.40	[e] # 8

[a] CIEMAT (2022)
[b] Schatz et al. (2013)
[c] Schatz and Akhanoba (2017)
[d] Pont and Idiart (2022)
[e] Hedström et al. (2023)

Table 5-2 shows the relative error (%) yielded by the model with respect to the experimental measurements. Overall, expansion has a considerably bounded error, whereas erosion shows a higher deviation in most cases. However, one should consider that in some cases, significant errors correspond to mass amounts that could perfectly be within the measurement error or experimental uncertainty. Also, it should be noted that the presented numerical model is still under development.

Table 5-2. Error (%) yielded by the model respect to the corresponding experimental measurements.

#case	Expansion radius [%]	Extruded mass [%]	Eroded mass [%]
Case 1	6.70	74.92	0.0
Case 2	2.81	12.09	0.0
Case 3	6.00	11.83	0.0
Case 4	-	-	0.0
Case 5	-	-	0.0
Case 6	-	-	0.0
Case 7	7.40	53.96	39.39
Case 8	8.48	75.14	30.69
Case 9	17.79	26.30	29.58
Case 10	-	-	-
Case 11	6.89	29.91	77.70
Case 12	7.34	16.11	84.91
Case 13	1.81	8.46	-
Case 14	-	57.75	12.05
Case 15	7.92	42.27	13.47
Case 16	-	-	38.55
Case 17	-	-	9.46
Case 18	-	-	3.19
Case 19	55.16	6.81	36.00
Case 20	5.84	-	40.00
Case 21	18.29	-	215.38
Case 22	2.33	21.35	71.04
Case 23	18.39	92.78	73.80
Case 24	0.0	35.33	40

6 Upscaling to repository conditions

6.1 Long-term buffer erosion rate for single horizontal fractures

For the upscaling to repository scale the parametrization of Nanocor bentonite has been considered. As expected, based on the preliminary results obtained by Pont (2022), Table 6-1 shows that in all cases the predicted erosion rate is significantly lower than the values provided by the upscaling of small-scale tests proposed by Smith et al. (2017). Another important outcome of the study is the prediction of the final bentonite expansion distance. In all cases expansion stops within 3.5 cm away from the buffer-fracture interface due to the effect off wall friction. It is important to state that the performance of the model at this scale cannot be validated against experimental data.

Table 6-1. Erosion rate after reaching pseudo-steady (g/year) in a single horizontal fracture.

	δ_1			δ_2			δ_3		
	c_1	c_2	c_3	c_1	c_2	c_3	c_1	c_2	c_3
v_1	0.45	0.63	0.88	2.52	2.15	1.54	6.70	5.55	3.89
v_2	1.25	1.26	1.54	4.16	5.11	6.33	16.65	12.49	11.50
v_3	1.99	2.17	2.71	7.42	8.39	9.70	23.72	22.20	21.63

From the data compiled in Table 6-1, a square root correlation between the erosion rate (g/year) and the fracture flow velocity v (m/s) has been found, as well as a quasi-quadratic dependence on the fracture aperture δ (m). Regarding the former, it nearly fits with the regression performed by Moreno et al. (2010) on its own expansion and erosion model, which found a dependency on $v^{0.41}$, whereas the analytical expressions derived by Neretnieks et al. (2010) using the Q_{eq} concept and Neretnieks et al. (2017) in his two-region model for a single bentonite buffer intersected by a horizontal fracture with water of glacial origin yielded also a square root correlation. This constitutes a major change from the previous version of the model, which used to rely on the Stokes equations and yielded a linear correlation.

On the other hand, the two previous models provided a linear correlation between erosion rate and fracture aperture, whereas the present model yields a quasi-quadratic one, which can be attributed to the effect of the wall friction term.

In terms of the sodium concentration at the bentonite-water interface, the model update accounting for a correlation between wall friction and this variable has led to an improved estimation of the erosion rate in the 1-8 mM range for wide fractures. However, the correlation becomes unclear with narrowing fracture apertures due to numerical issues related to the rim tracking algorithm presented by Pont (2023). Due to the size of the model, the resolution of the computational mesh is lower than in the small-scale cases, for which a small misplacement of the rim in terms of smectite concentration can lead to a significant miscalculation of the erosion rate in the long term. This issue is further discussed in Section 7.

6.2 Long-term buffer erosion rate for single vertical fractures

As expected, the erosion rate in the buffer geometry with a single intersecting vertical fracture is larger than in the equivalent horizontal geometry. Also, an unclear correlation between erosion rate and sodium concentration at the rim has been obtained. This is mainly due to the widest fracture aperture considered being 0.4 mm.

The correlation between erosion rate and fracture aperture shows a slightly different behavior from the horizontal case. It behaves quadratically near the lower limit (0.1 mm) and slowly becomes cubic when increasing the fracture aperture. It is consistent with the particle aggregate size correlation presented in equation 6c.

Table 6-2. Erosion rate after reaching pseudo-steady (g/year) in a single vertical fracture.

	c_1	c_2	c_3
δ_1	0.46	0.46	0.46
δ_2	1.05	1.03	1.08
δ_3	15.80	11.70	15.80

7 An updated equation for the long-term buffer erosion rate for single horizontal fractures

The present section is fully devoted to addressing the numerical issues observed in Section 5 in terms of the correlation between long-term erosion rate and sodium concentration in large-scale bentonite buffer geometries intersected by a single horizontal fracture. To this purpose, the finite element mesh was further refined on the bentonite-water interface, which subsequently increased the accuracy of the rim-tracking algorithm (Pont, 2023) for a proper placement of the wall friction boundary term presented in Section 3.1.

Table 7-1 presents the results in terms of long-term erosion rate ER (g/y) for the 27 cases corresponding to the parametrization described in Section 5, which includes three different values for fracture aperture, sodium concentration and fracture flow velocity. Moreover, the results provided by the present numerical model are compared to those obtained with the semi-empirical expression derived by Neretnieks et al. (2017).

Table 7-1. Erosion rate after reaching pseudo-steady (g/y) in a single horizontal fracture calculated with a semi-empirical expression (left) and with the present model (right).

		Semi-empirical expression (KTH)				**A21 model**			
			[Na] (mM)				**[Na] (mM)**		
		Veloc. (m/s)	**1**	**4**	**8**	**Veloc. (m/s)**	**1**	**4**	**8**
Fracture aperture (mm)	1	1E-06	14.71	1.55	1.48	1E-06	12.40	3.98	3.76
		5E-07	10.40	1.09	1.04	5E-07	8.40	2.60	2.47
		1E-07	4.65	0.49	0.47	1E-07	3.36	1.11	1.03
	0.6	1E-06	8.81	0.93	0.88	1E-06	7.18	2.09	2.14
		5E-07	6.23	0.65	0.62	5E-07	4.92	1.38	1.43
		1E-07	2.79	0.29	0.28	1E-07	2.03	0.58	0.60
	0.2	1E-06	2.93	0.31	0.29	1E-06	2.46	0.67	0.65
		5E-07	2.07	0.22	0.21	5E-07	1.69	0.45	0.45
		1E-07	0.93	0.10	0.09	1E-07	0.67	0.20	0.19

For a better visualization of the results, Figure 7-1 shows the correlation between erosion rate and sodium concentration, which was the main struggle for the model in Section 5. Overall, the model reproduces the main trends of the semi-empirical expression, including the plateau observed between 4 and 8 mM. Also, both methods capture a steep decrease in the erosion rate when increasing sodium concentration from 1 to 4 mM. For all considered apertures and velocities, the erosion rates at 1 mM sodium are very similar in both approaches. However, the present model is more conservative for higher sodium concentrations. This slight disagreement can be attributed to the fact that the calibration of model has mostly been carried out with small-scale tests using 1 mM NaCl solutions. Finally, it can also be concluded that the effect of wall friction on expansion (few centimeters in all cases) is much stronger than on the erosion rate.

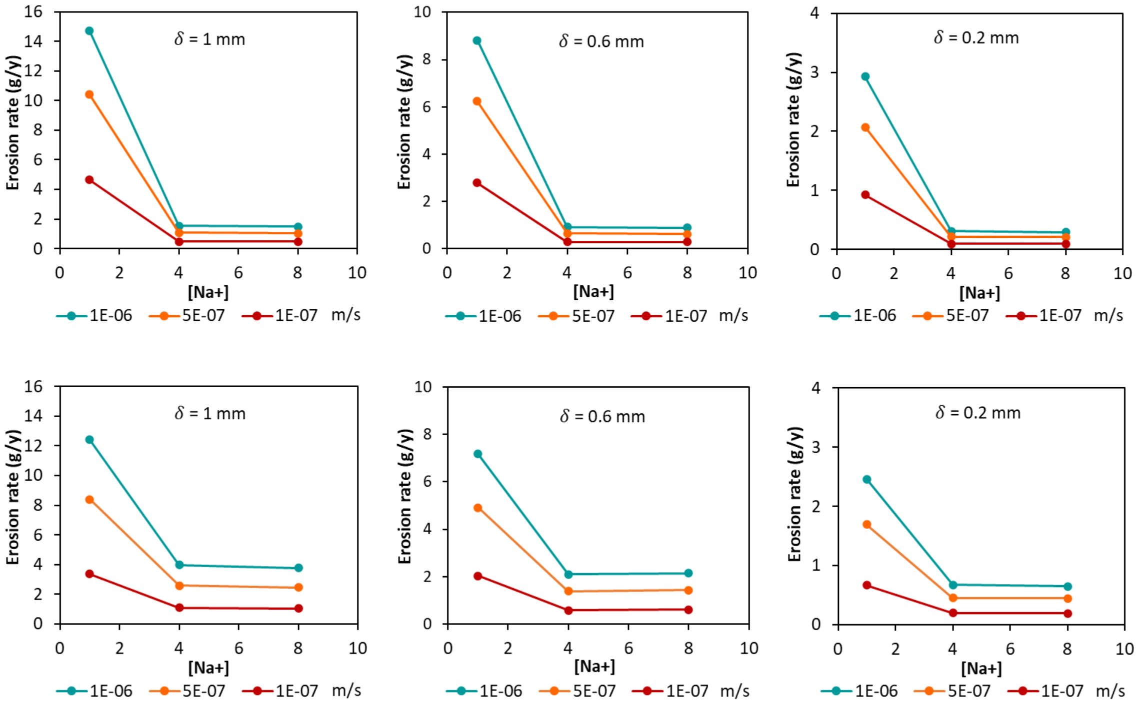

Figure 7-1. Bentonite erosion rate correlation with sodium concentration for different flow velocities and fracture apertures. (Top) results obtained with a semi-empirical expression (Neretnieks et al., 2017), (bottom) model results.

The data presented in Table 7-1 has been transformed into a multivariable non-linear regression equation that can be used to predict the long-term erosion rate in one KBS-3 deposition hole intersected by a single horizontal fracture. It should be noted that, in terms of sodium concentration, the use of Equation 7 should be restricted to the range of 1-8 mM and to MX-80 bentonite.

$$ER\ (\text{g/y}) = 7.03 \cdot 10^3 D v^{0.5} \delta^{1.2} [\text{Na}]^{-0.7} \qquad (7)$$

where D(m) is the diameter of the bentonite buffer (1.75 m for the KBS-3 concept), δ(m) is the fracture aperture and v(m/s) is the inlet flow velocity. The square-root correlation with the latter is consistent with the experimentally based regressions performed by Moreno et al. (2010) and Neretnieks et al. (2017). In terms of fracture aperture, the correlation is slightly stronger than linear. This can be attributed to wall friction and could thus explain the extremely low erosion rates observed in 0.1 mm fractures by Hedström et al. (2023). Finally, the accuracy of the regression procedure is shown in Figure 7-2.

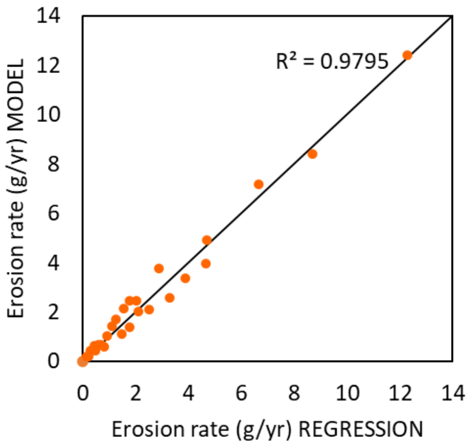

Figure 7-2. Regression error of Equation 7.

8 Conclusions and future work

The new version of the model accounts for a correlation between wall friction and sodium concentration at the bentonite-water interface, which allows reproducing a thicker sol region when salinity decreases and thus providing more realistic erosion rates. This has led to a positive outcome regarding the simulation of the small-scales tests that had already been modeled by Pont (2023). The results shown in Section 5 show a significant quantitative improvement in terms of the adjustment of the eroded mass for three different kind of bentonites and a wide range of fracture apertures flow regimes.

The refinement of the sedimentation model considering a cubic law for fractures wider than 0.1 mm, and a quadratic correlation between particle aggregate velocity and size for the rest, has also led to a significantly more realistic reproduction of expansion and erosion in sloping fractures. In spite of not dealing with discrete particle mechanics, the model has been able to reproduce the transient nature of sedimentation observed by Leal Olloqui et al. (2024) and Hedström et al. (2023) in 0.1 mm fractures. However, the drastic reduction of mass loss rate in similar cases with fracture flow has not been reproduced by the model, for which it can be concluded that the interaction between flow erosion and gravity must be further studied. The generation of colloids, which is the main sedimentation and erosion driver, should be further investigated in vertical narrow fractures, where the colloidal concentration might reach an equilibrium.

After the current model extension, the predicted long-term erosion rate for the KBS-3 buffer concept intersected by a single horizontal fracture has been significantly lower than the upscaling from small-scale tests performed by Smith et al. (2017) in all considered cases. On the other hand, despite obtaining a significant improvement, the results still show an unclear correlation between erosion rate and sodium concentration in the fracture water, which contrasts with the drastic mass loss increase observed experimentally when sodium concentration tends to zero. This disagreement has been attributed to the accuracy of the rim tracking algorithm presented by Pont (2023), which has specially struggled to properly place the bentonite-water interface in narrow fractures. This issue should be addressed in the next model development phase, since a wrong location of this boundary strongly penalizes the long-term accuracy of the erosion rate estimate. On the other hand, the correlations between long-term erosion rate and flow velocity and fracture aperture have led to interesting outcomes. Regarding the former, the use of Darcy's law as flow model for the integration of the sedimentation model (Section 3.2) has changed the linear correlation obtained by Pont (2023) to a square root one as predicted by Moreno et al. (2010) and Neretnieks et al. (2017), whereas the latter has remained quadratic due to the effect of the wall friction term.

The model has also been applied to a KBS-3 buffer intersected by a single vertical fracture considering a fixed inlet flow velocity. Again, the correlation with sodium concentration has not been properly reproduced due to the issue pointed in the previous paragraph. The correlation between erosion rate and fracture aperture shows a different behavior from the horizontal case. It behaves quadratically near the lower limit (0.1 mm) and slowly becomes cubic when increasing the fracture aperture, which is consistent with the implemented particle aggregate size correlation.

In Section 7, the numerical issues observed in Section 5 in terms of the correlation between the long-term bentonite erosion rate and sodium concentration have been solved. With that, a regression equation based on flow velocity, fracture aperture and sodium concentration has been derived for a KBS-3 deposition hole intersected by a single horizontal fracture, obtaining similar outcomes to the semi-empirical expression derived by Neretnieks et al. (2017). The main difference is the effect of wall friction, which has limited expansion to few centimeters and has led to a correlation between erosion rate and fracture aperture slightly stronger than linear.

9 References

SKB's (Svensk Kärnbränslehantering AB) publications can be found at www.skb.com/publications. SKBdoc documents will be submitted upon request to document@skb.se.

Adachi Y, Nakaishi K, Tamaki M, 1998. Viscosity of dilute suspension of sodium montmorillonite in an electrostatically stable condition. Journal of Colloid and Interface Science, 198, pp 100–105.

Arthur R, 2011. Handling of hydrogeochemical relations in erosion and swelling pressure models for the buffer and backfill. Part I: A review of surface-chemical concepts used in models of buffer erosion. STUK-TR 10, Radiation and Nuclear Safety Authority (STUK).

COMSOL, 2023. COMSOL Multiphysics® v. 6.1 www.COMSOL.com. COMSOL AB,

CIEMAT, 2022. BENERO, bentonite erosion Project. Internal report.

Hedström M, Nilsson U, Lamminmaki R, 2023. Experimental study of montmorillonite erosion in low ionic strength water under stagnant and flow conditions in artificial fractures. Applied Clay Science 239, 106929.

Leal Olloqui M, Sellin P, Kronberg H, Bladström T, 2024. Exploring bentonite sedimentation dynamics 2019-2021. SKB P-23-21, Svensk Kärnbränslehantering AB.

Liu L, Moreno L, Neretnieks I, 2009. A dynamic force balance model for colloidal extrusion and its DLVO-based application. Langmuir, 25, 679-687. https://doi.org/10.1021/la8026573

Liu L, Neretnieks I, 2006. Physical and chemical stability of the bentonite buffer. SKB R-06-103, Svensk Kärnbränslehantering AB.

Moreno L, Neretnieks I, Liu L, 2010. Modelling of erosion of bentonite gel by gel/sol flow. SKB TR-10-64, Svensk Kärnbränslehantering AB.

Neretnieks I, Liu L, Moreno L, 2009. Mechanisms and models for bentonite erosion. SKB TR-09-35, Svensk Kärnbränslehantering AB.

Neretnieks I, Liu L, Moreno L, 2010. Mass transfer between waste canister and water seeping in rock fractures. Revisiting the Q-equivalent model, SKB TR-10-42, Svensk Kärnbränslehantering AB.

Neretnieks I, Moreno L, 2018. Some mechanisms that influence bentonite erosion in a KBS-3 repository – an exploratory study. SKB TR-18-13, Svensk Kärnbränslehantering AB.

Neretnieks I, Moreno L, Liu L, 2017. Clay erosion – impact of flocculation and gravitation. SKB TR-16-11, Svensk Kärnbränslehantering AB.

Ponce V M, 2017. Vlab, Online Calculations (https://ponce.sdsu.edu). San Diego State University (USA).

Pont A, Coene E, Idiart A, 2020. Bentonite erosion project. Preliminary study for the numerical simulation of bentonite erosion. SKB P-20-16, Svensk Kärnbränslehantering AB.

Pont A, Idiart A, 2022. POSKBAR-Bentonite Erosion Project. Numerical Model for the Quantification of Buffer Bentonite Mass Losses due to Expansion, Erosion and Sedimentation. Posiva SKB Report 13, Svensk Kärnbränslehantering AB & Posiva.

Pont A, 2023. POSKBAR-Bentonite Erosion Project. Optimization and validation of a model for quantifying bentonite buffer mass losses due to expansion, erosion, and sedimentation. SKB P-23-03. Svensk Kärnbränslehantering AB.

Pujala R K, 2014. Dispersion stability, microstructure and phase transition of anisotropic nanodiscs. Cham, Switzerland: Springer International Publishing.

Schatz T, Akhanoba N, 2017. Bentonite Buffer Erosion in Sloped Fracture Environments. Posiva 2016-13, Posiva Oy.

Schatz T, Kanerva N, Martikainen J, Sane P, Olin M, Seppälä A, Koskinen K, 2013. Buffer Erosion in Dilute Groundwater. Posiva 2012-44, Posiva Oy.

Sena C, Salas J, Arcos D, 2010. Aspects of geochemical evolution of the SKB near field in the frame of SR-Site. SKB TR-10-59, Svensk Kärnbränslehantering AB.

SKB, 2004. Interim process report for the safety assessment SR-Can. SKB R-04-33. Svensk Kärnbränslehantering AB.

SKB, 2006. Long-term safety for KBS-3 repositories at Forsmark and Laxemar – a first evaluation. Main Report of the SR-Can project. SKB TR-06-09, Svensk Kärnbränslehantering AB.

SKB, 2011. Long-term safety for the final repository for spent nuclear fuel at Forsmark. Main report of the SR-Site project. SKB TR-11-01. Svensk kärnbränslehantering AB.

Smith P, Schatz T, Reijonen H, Hellä P, 2017. Chemical Erosion and Mass Redistribution of Bentonite in a KBS-3H Repository. Posiva 2016-12, Posiva Oy.

Appendix A

The equations of the KTH model corresponding to the derivation of the smectite diffusion coefficient (Liu et al., 2009), which have been implemented in COMSOL, are presented below:

$$\partial_t \varphi = -\vec{u} \nabla \varphi + \nabla \cdot (D_F \nabla \varphi) \qquad \text{A-1}$$

$$D_F = \frac{\chi}{f} \qquad \text{A-2}$$

$$h = \left(\frac{\varphi_{max}}{\varphi} - 1\right) \delta_p \qquad \text{A-3}$$

$$f = \left[6\pi\eta_w r_{eq} + V_p k_0 \tau^2 a_p^2 \eta_w \frac{\varphi}{(1-\varphi)^2}\right] \qquad \text{A-4}$$

$$\chi = k_B T + \left(h + \delta_p\right)^2 \left(\frac{\partial F_A}{\partial h} - \frac{\partial F_R}{\partial h}\right) \qquad \text{A-5}$$

$$\frac{\partial F_A}{\partial h} = -\frac{A_H S_p}{2\pi}\left[h^{-4} - 2\left(h + \delta_p\right)^{-4} + \left(h + 2\delta_p\right)^{-4}\right] \qquad \text{A-6}$$

$$\frac{\partial F_R}{\partial h} = -4\kappa c R T S_p \tanh y^m \left[\cosh y_\infty^m \sinh\left(\frac{y_\infty^m}{2}\right) + \frac{1}{\kappa h}\sinh y_\infty^h + \frac{2}{(\kappa h)^2}\sinh\left(\frac{y_\infty^h}{2}\right)\right] \qquad \text{A-7}$$

$$y^m = \operatorname{asinh}\left[2\sinh y_\infty^m + \frac{4}{\kappa h}\sinh\left(\frac{y_\infty^h}{2}\right)\right] \qquad \text{A-8}$$

$$y_\infty^m = 4\operatorname{atanh}\left[\tanh\left(\frac{y_\infty^0}{4}\right)\exp\left(-\frac{\kappa h}{2}\right)\right] \qquad \text{A-9}$$

$$y_\infty^h = 4\operatorname{atanh}\left[\tanh\left(\frac{y_\infty^0}{4}\right)\exp(-\kappa h)\right] \qquad \text{A-10}$$

$$\kappa = \left(\frac{2F^2 c z^2}{\varepsilon_0 \varepsilon_r R T}\right)^{1/2} \qquad \text{A-11}$$

$$y_\infty^0 = 2\operatorname{asinh}\left(\frac{s_0}{2}\right) \qquad \text{A-12}$$

$$s_0 = \frac{z F \sigma^0}{\varepsilon_0 \varepsilon_r \kappa R T} \qquad \text{A-13}$$

The smectite sol viscosity correlation presented by Adachi et al. (1998) has also been implemented:

$$\eta_{rel} = 1 + 1.022\varphi_{cov} + 1.358\varphi_{cov}^3 \qquad \text{A-14}$$

$$\varphi_{cov} = \frac{2}{3}\frac{\left(D_P + 2m\kappa^{-1}\right)^3}{D_p^2 \delta_p} \qquad \text{A-15}$$

Notation	**Property**	**Value and/or unit**
k_B	Boltzmann's constant	$1.380 \cdot 10^{-23}$ J/K
r_{eq}	Equivalent radius of non-spherical particles	63.66 nm
F	Faraday's constant	96 485 C/mol
m	Fitting parameter in co-volume fraction	1
R	Gas constant	8.314 J/(K mol)
A_H	Hamaker constant	$2.5k_B$T
$k_0\tau^2$	Kozeny's constant	5.13
φ_{max}	Maximum volume fraction of smectite	1
ε_0	Permittivity of vacuum	$8.854 \cdot 10^{-12}$ F/m
ε_r	Relative permittivity of water	78.54
D_P	Smectite particle diameter	200 nm
δ_p	Smectite particle thickness	1 nm
a_p^2	Specific surface area per unit volume of particles	$2/\delta_p$ m^2/ m^3
S_p	Surface area of smectite particle	$3.1415 \cdot 10^{-14}$ m^2
σ^0	Surface charge of particles	-0.131 C/m^2
T	Temperature	298.15 K
z	Valence of counterion	1
η_w	Viscosity of water	$1.002 \cdot 10^{-3}$ N s/m^2
φ	Volume fraction of smectite – variable	-
V_p	Volume of the smectite particles	$3.1415 \cdot 10^{-23}$ m^3